Vanadium-based superconductivity in the breathing kagome compound $Ta_2V_{3.1}Si_{0.9}$

HongXiong Liu,[1,2,*] JingYu Yao,[1,3,*] JianMin Shi,[4,*] ZhiLong Yang,[1] DaYu Yan,[1] Yong Li,[1,2] DaiHong Chen,[4] Hai L. Feng,[1,5] ShiLiang Li,[1,3,5] ZhiJun Wang,[1,3,†] and YouGuo Shi[1,2,5,‡]

[1]*Beijing National Laboratory for Condensed Matter Physics and Institute of Physics, Chinese Academy of Sciences, Beijing 100190, China*
[2]*Center of Materials Science and Optoelectronics Engineering, University of Chinese Academy of Sciences, Beijing 100190, China*
[3]*School of Physical Sciences, University of Chinese Academy of Sciences, Beijing 100190, People's Republic of China*
[4]*Ningbo Fengcheng Advanced Energy Materials Research Institute Co., Ltd., Ningbo 315000, China*
[5]*Songshan Lake Materials Laboratory, Dongguan, Guangdong 523808, China*

(Received 25 June 2023; revised 10 August 2023; accepted 29 August 2023; published 13 September 2023)

Superconductivity in V-based kagome metals has recently raised great interest as they exhibit the competing ground states associated with the flat bands and topological electronic structures. Here we report the discovery of superconductivity in $Ta_2V_{3.1}Si_{0.9}$ with a superconducting transition temperature T_c of 7.5 K, a record high for kagome metals at ambient pressure. While the V ions form a two-dimensional breathing kagome structure, the length difference between two different V-V bonds is just 0.05 Å, making it very close to the perfect kagome structure. Our results show that $Ta_2V_{3.1}Si_{0.9}$ is a moderate-coupled type-II superconductor with a large upper critical field that is close to the Pauli limit. DFT calculations give a Van Hove singularity band located at Fermi energy, which may explain the relatively high T_c observed in this material. Furthermore, electron-phonon coupling calculations indicate that the in-plane vibrations of the V atoms play a significant role in driving the superconductivity.

DOI: 10.1103/PhysRevB.108.104504

I. INTRODUCTION

The kagome lattice, consisting of the layered structure formed by corner-sharing triangles, has garnered extensive attention in condensed matter physics. Kagome antiferromagnetic insulators are one of the ideal platforms to explore the long-sought quantum-spin-liquid states [1–7]. Kagome metals host intriguing physics as well due to the inherent Dirac cones, Van Hove singularities (VHSs), and flat bands at different electron fillings in their electronic structures [8]. Interestingly, theoretical studies have suggested that unconventional superconductivity can be realized in the kagome lattice within a special range of on-site repulsion and Coulomb interaction at Van Hove filling, where the Fermi surfaces are nested and have saddle points on the edges of the Brillouin zone [9,10]. However, the emergence of superconductivity is still rare in kagome metals.

A recently discovered family of materials with a V-based kagome lattice, AV_3Sb_5 (A = K, Rb, and Cs) [11], exhibits superconductivity with the superconducting transition temperature T_c = 0.93, 0.92, and 2.5 K for K, Rb, and Cs variants, respectively [12–14]. Moreover, many interesting phenomena have also been discovered, such as anomalous Hall effect [15], unconventional chiral CDW order [16–18], and topologically nontrivial band structures [12,19]. In the superconducting phase of CsV_3Sb_5, while the Hebel-Slitchter coherence peak observed in nuclear magnetic resonance [20] and temperature-dependent magnetic penetration depth [21] measurements reveal the feature of a conventional s-wave superconductor, an unconventional superconducting state has been suggested by other results, such as a finite residual linear term of thermal conductivity at zero magnetic field [22], residual zero-energy density of states (DOS) [23,24], and the observation of pair density wave (PDW) [25]. And these seemingly experimental conflictions may be resolved in a time-reversal symmetry-breaking PDW scenario that arises from the interplay between PDW and a nested Fermi surface [26].

Superconductivity also arises in kagome lattice made up of 4d or 5d elements, such as ternary Laves phase Mg_2Ir_3Si [27] and RT_3X_2 series (R = lanthanide, T = 4d or 5d transition metal, and X = Si, B, or Ga) [28–34], where transition metals host an isolated perfect or distorted kagome lattice. In contrast, Sb atoms at the 1a site of AV_3Sb_5 are located in the center of the V kagome lattice. Therefore, the realization of an isolated V-based kagome lattice is an attractive challenge and may provide intensive insight into the novel phenomena observed in the AV_3Sb_5 family.

In this work, we synthesized a V-based breathing kagome superconductor, $Ta_2V_{3.1}Si_{0.9}$, with a T_c of 7.5 K. The difference in the side length of the corner-sharing triangles is a mere 2%. A moderate-coupled type-II superconductivity is confirmed by the comprehensive measurement of magnetism, resistivity, and specific heat. Interestingly, the large upper critical field is close to the Pauli limit, suggesting unconventional behavior exists. DFT calculations indicate that a VHS band mainly from the V-d_{yz} states is located at the Fermi energy, which is strongly relevant to the emergence of the

*These authors contributed equally to this work.
†Corresponding author: wzj@iphy.ac.cn
‡Corresponding author: ygshi@iphy.ac.cn

superconductivity. The electron-phonon coupling calculation further unveils that the in-plane vibrations of V atoms mainly contribute to the superconductivity.

II. EXPERIMENT DETAILS

Polycrystalline samples of $Ta_2V_{3.1}Si_{0.9}$ were synthesized by using the arc-melting method. High-quality ingredients Ta (Tangchuan Sci-Tech Co., Ltd, 3N, 5.913g), V (Innochem, 3N, 2.58g), and Si (Alfa, 4N, 0.413g) were weighed out in a molar ratio of 2: 3.1: 0.9, arc-melted thrice under argon an atmosphere, utilizing a titanium ingot as an oxygen getter. The sample was then annealed in a vacuumed quartz tube at the temperature of 1073 K for 3 days. The polycrystalline ingot was silvery and stable in the air. Rectangular-shaped samples were obtained for physical property measurements by using the diamond wire-cutting machine.

The powder x-ray diffraction (PXRD) on crushed samples was performed in Rigaku SmartLab 9 kW with Cu $K\alpha$ radiation. The crystal structure was refined with the program package GSAS-II suite [35]. Magnetic susceptibility $\chi(T) = M/H$ and isothermal magnetization $M(H)$ were measured using a Physical Property Measurement System (PPMS Dynacool, Quantum Design) equipped with a vibrating sample magnetometer (VSM) option. A sample weighing 14 mg was chosen for heat capacity measurement in the same PPMS. The standard four-probe method was employed for electric measurement in PPMS-16T.

The calculations of the electronic band structure were performed using the Vienna *ab initio* package (VASP) with projector augmented wave (PAW) method and Perdew-Burke-Ernzerhof (PBE) exchange-correlation functional. A plane wave energy cutoff of 420 eV and a $16 \times 16 \times 10$ k mesh were employed. We adopted the virtual crystal approximation (VCA) to simulate $Ta_2V_{3.1}Si_{0.9}$ with 10% V and 90% Si at the 2a Wyckoff site. The phonon spectrum and electron-phonon coupling calculations of $Ta_2V_{3.1}Si_{0.9}$ were performed in the framework of density functional perturbation theory, as implemented in the QUANTUM ESPRESSO (QE) package. To simulate the doping effect, we added 1.8 electrons and a compensating jellium background into the Ta_2V_3Si system in QE. The superconducting temperature was evaluated with Allen-Dynes modified McMillian equation using QE.

III. RESULTS AND DISCUSSION

$Ta_2V_{3.1}Si_{0.9}$ crystallizes in a hexagonal Mg_2Cu_3Si-type structure, which is also referred to as the ternary C14 Laves phase. The Rietveld refinement of the powder sample, as shown in Fig. 1(c), results in the space group $P6_3/mmc$ (no. 194) with cell parameters of $a = 5.0094(8)$ Å and $c = 8.2575(1)$ Å, which is consistent with the structure of Ta_2V_3Si reported previously [36]. A small amount of unknown impurity phase is detected in the powder sample. The atomic coordinates, occupancies, and isotropic displacement parameters are listed in Table I. The structure of $Ta_2V_{3.1}Si_{0.9}$ consists of Ta_2Si layers and V breathing kagome layers stacking along the crystallographic c axis, as shown in Fig. 1(a). The extra V atoms occupy the 2a site of Si atoms. Figure 1(b) shows the breathing kagome net of V atoms, in which the shorter

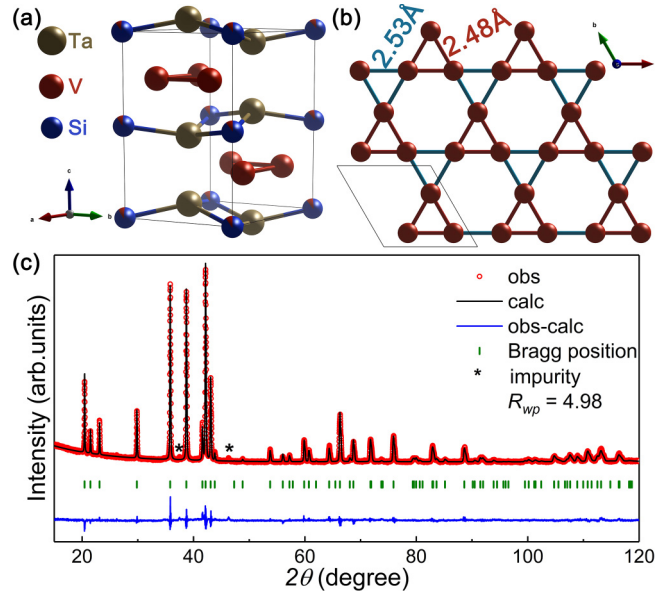

FIG. 1. Crystal structure of $Ta_2V_{3.1}Si_{0.9}$. (a) The side view of the crystal structure of $Ta_2V_{3.1}Si_{0.9}$. (b) The breathing kagome lattice of V atoms viewed from the crystallographic c axis. The structure is drawn in the program VESTA [37]. (c) The powder XRD pattern and refined results. The red circles and black lines are observed data and calculated patterns. The green sticks and blue lines represent the Bragg position and the difference between observed and calculated patterns.

and longer distances of the V-V bonds are 2.48 and 2.53 Å, respectively. The difference between the two kinds of V-V bonds is only 2%. The bond length of the kagome net here is much shorter than those observed in the analogous superconductors, including KV_3Sb_5 (2.74 Å, V-V bond) [11], $LaRu_3Si_2$ (2.84 Å, Ru-Ru bond) [30], and Mg_2Ir_3Si (2.62 and 2.73 Å, Ir-Ir bond) [27]. Considering a naive perspective that pressure may enhance the critical temperature, the shorter V-V bond in $Ta_2V_{3.1}Si_{0.9}$, seemingly pressing the sample along the kagome plane, implies a higher critical temperature. Moreover, compared with the V-based kagome superconductors AV_3Sb_5 [12–14], $Ta_2V_{3.1}Si_{0.9}$ exhibits the pure kagome plane without any other atoms, making it highly suitable for studying kagome physics.

The superconductivity of $Ta_2V_{3.1}Si_{0.9}$ is first confirmed by the volume magnetic susceptibility ($4\pi\chi$) measurements

TABLE I. Crystallographic data for $Ta_2V_{3.1}Si_{0.9}$ at room temperature. Space group $P6_3/mmc$ (no. 194), $a = 5.0094(8)$ Å, $c = 8.2575(1)$ Å, $V = 179.45(9)$ Å^3.

Atom	x	y	z	Site	Occ.[a]	U_{iso}[b]
Ta	1/3	2/3	0.5603(7)	4f	1	0.01
V1	0.1682(2)	0.3364(5)	1/4	6h	1	0.0077
V2	0	0	0	2a	0.1	0.0098
Si	0	0	0	2a	0.9	0.0098

[a]The occupancy of each atom.
[b]The isotropic displacement parameters are used to avoid an unphysical negative value.

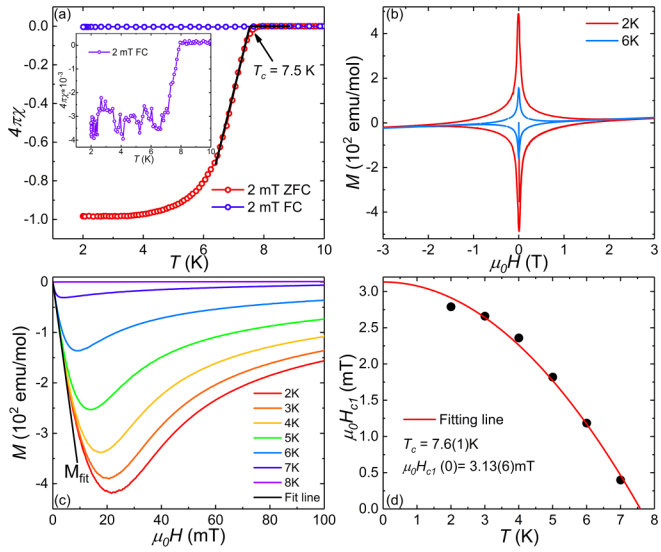

FIG. 2. The magnetic characterization of $Ta_2V_{3.1}Si_{0.9}$. (a) The temperature-dependent magnetic susceptibility under a magnetic field of 2 mT with ZFC and FC modes (the inset shows the enlarged view of FC data). (b) The field-dependent magnetization at 2 and 6 K from −3 to 3 T. (c) The field-dependent magnetization from 2 to 8 K in an increment of 1 K at low magnetic fields. (d) The lower critical field $\mu_0 H_{c1}$ versus temperature and the fitting using empirical relation.

under zero-field-cooled (ZFC) and field-cooled (FC) modes from 2 to 10 K with an external magnetic field of 2 mT, as shown in Fig. 2(a). The critical temperature (T_c) of 7.5 K is determined from the intersection between the extrapolated normal state of magnetic susceptibility at low temperature and the line representing the apparent diamagnetic signal (shown by the black lines) [38,39]. The superconducting volume fraction reaches almost 100% in the ZFC data. Generally, the $4\pi\chi$ should exceed 100% for the reason of the demagnetization effect. The lower superconducting volume fraction can be attributed to the existence of trace impurities detected in the powder XRD patterns. The weak diamagnetic signal observed in the FC process, as shown in the inset of Fig. 2(a), ascribes to the polycrystalline nature of the sample and also the flux pinning effect in a type-II superconductor, which is explicitly verified by the loops in isothermal magnetization at 2 and 6 K, shown in Fig. 2(b). Figure 2(c) depicts the detailed investigation of the field-dependent magnetization $M(H)$ performed at temperatures from 2 to 8 K with an interval of 1 K. To obtain the lower critical field, $\mu_0 H_{c1}$, the low-field data of 2 K are fitted linearly (indicated by the black solid line), and the $\mu_0 H_{c1}$ is defined where the data begin to deviate from the fitting line. The extracted $\mu_0 H_{c1}$ of each temperature are shown in Fig. 2(d) and fitted by using the empirical equation

$$\mu_0 H_{c1}(T) = \mu_0 H_{c1}(0)\left[1 - \left(\frac{T}{T_c}\right)^2\right],$$

where the fitting parameter $\mu_0 H_{c1}(0)$ is the lower critical field at 0 K and T_c is the superconducting transition temperature. The fit yields $\mu_0 H_{c1}(0)$ is 3.13(6) mT and T_c is 7.6(1) K, basically coinciding with the critical temperature observed in the $4\pi\chi(T)$ curve.

The temperature-dependent resistivity $\rho(T)$ measured from 300 to 2 K is shown in the inset of Fig. 3(b). The sample exhibits metallic behavior above the superconducting transition with a large residual resistivity of almost 0.4 mΩ cm. The low-temperature resistivity fitted by the equation $\rho(T) = \rho_0 + AT^n$, where ρ_0 is the residual resistivity and A and n are fitting parameters, yields that ρ_0 is 0.398 mΩ cm, A is $1.1(2) \times 10^{-6}$, and n is 1.91(4). The value of n close to 2 implies that electron-electron interaction dominates the low-temperature resistivity. Figure 3(a) shows $\rho(T)$ from 2 to 11 K under the increased magnetic field to 15 T with an increment of 1 T. The T_c, defined as the temperature where the resistivity drops to 50% of the normal state (ρ_N), is 8.1 K. The T_c shifts to the lower temperature with increased fields. Using the 50% intersection criteria of T_c for determining the upper critical field ($\mu_0 H_{c2}$), a general criterion for $\mu_0 H_{c2}$, we obtain the temperature-dependent $\mu_0 H_{c2}(T)$ in Fig. 3(b). The slope near T_c ($H' = -\frac{d\mu_0 H_{c2}}{dT}|_{T_c}$) is 3.05 T/K. This relatively large value gives a high orbital limiting field $\mu_0 H_{c2}^{\rm orb}(0)$ to be 17.12 T, which is determined from $\mu_0 H_{c2}^{\rm orb}(0) = -0.693 H' T_c$ in the dirty limit superconductor [40] (which will be proved later according to the larger mean free path rather than the Ginzburg-Landau coherence length). Generally, the Pauli-limited field $\mu_0 H_P(0)$ is $1.85 T_c$ (a common estimation for superconductors); using $T_c = 8.1$ K, the $\mu_0 H_P(0)$ is calculated to be 14.985 T. That the $\mu_0 H_P(0)$ is smaller than $\mu_0 H_{c2}^{\rm orb}(0)$ implies that $\mu_0 H_{c2}$ at low temperature is limited by the Pauli spin susceptibility of the electrons rather than the usual orbital pair-breaking effect, which suggests the anomalous property of the superconductor reported here.

To comprehensively investigate the pair-breaking mechanism in the material, we fit our data based on the Werthamer, Helfand, and Hohenberg (WHH) model [40,41]:

$$\ln\frac{1}{t} = \left(\frac{1}{2} + \frac{i\lambda_{\rm so}}{4\gamma}\right)\psi\left(\frac{1}{2} + \frac{\bar{h} + \frac{\lambda_{\rm so}}{2} + i\gamma}{2t}\right) + \left(\frac{1}{2} - \frac{i\lambda_{\rm so}}{4\gamma}\right)\psi\left(\frac{1}{2} + \frac{\bar{h} + \frac{\lambda_{\rm so}}{2} - i\gamma}{2t}\right) - \psi\left(\frac{1}{2}\right),$$

where $t = T/T_c$, $\gamma \equiv (\alpha\bar{h})^2 - (\lambda_{\rm SO}/2)^{21/2}$, ψ is the digamma function,

$$h^* \equiv \frac{\bar{h}}{\left(-\frac{d\bar{h}}{dt}\right)_{t=1}} = \frac{\pi^2\bar{h}}{4} = \frac{H_{c2}}{\left(-\frac{dH_{c2}}{dt}\right)_{t=1}},$$

and α (also known as the Maki parameter [42,43]) and $\lambda_{\rm so}$ are parameters presenting the strength of the spin paramagnetic effect and spin-orbit scattering. First, the data are fitted neglecting the spin paramagnetic effect and spin-orbit scattering ($\alpha = 0$ and $\lambda_{\rm so} = 0$), while the fitting line (green solid line) deviates the data at low temperatures. Considering the strong Pauli paramagnetic effect in this sample, we obtain the Maki parameter $\alpha = 1.62$ by substituting the calculated values of $\mu_0 H_{c2}^{\rm orb}(0)$ and $\mu_0 H_P(0)$ into the formula [43]:

$$\alpha = \frac{\sqrt{2} H_{c2}^{\rm orb}(0)}{H_p(0)}.$$

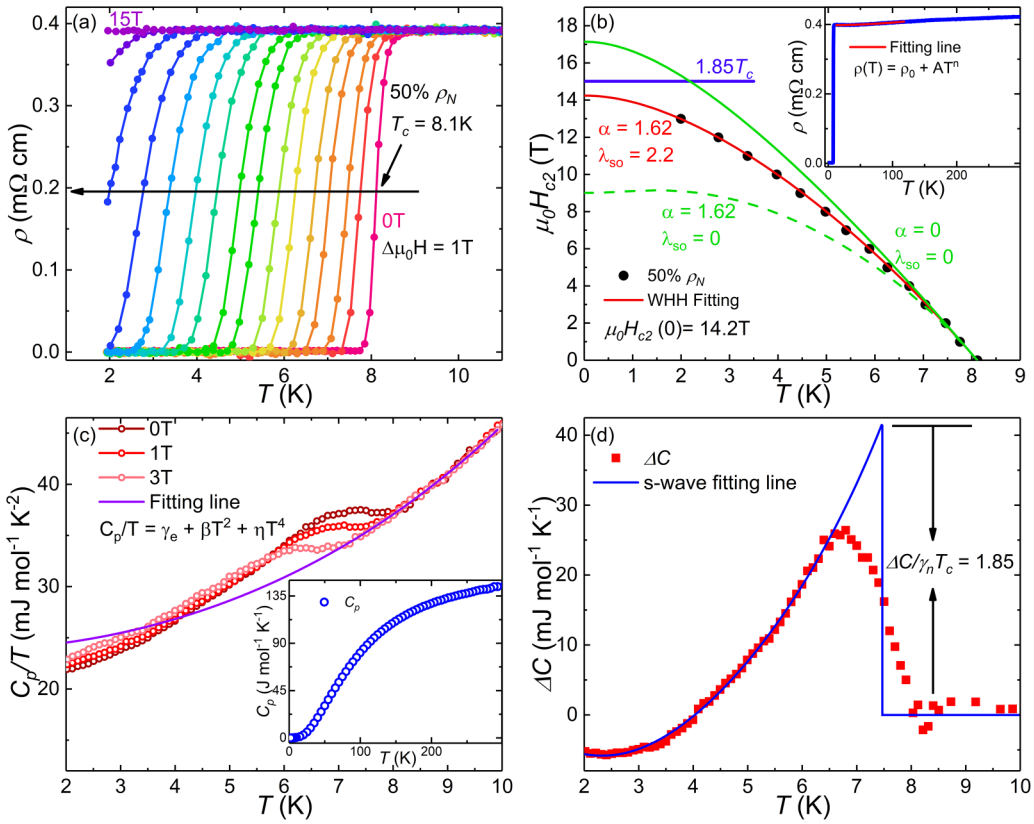

FIG. 3. The resistivity and specific heat of $Ta_2V_{3.1}Si_{0.9}$. (a) The temperature-dependent resistivity under magnetic field from 0 to 15 T in an increment of 1 T. (b) The upper critical field versus temperature data and the WHH fitting. The inset shows the temperature dependence of resistivity from 300 to 2 K. (c) The temperature-dependent specific heat under various magnetic fields. The inset illustrates the specific heat from 300 to 2 K. (d) ΔC versus T data from 10 to 2 K. The blue line below the critical temperature is the s-wave fitting.

By fixing the value of $\alpha = 1.62$ and adjusting the λ_{so}, the data can be well fitted by the WHH model (red solid line), yielding the $\mu_0 H_{c2}(0) = 14.2$ T. Noticing that the parameter $\lambda_{so} = 2.2$ is essential to depict the experiment data, and the fitting line ignoring the λ_{so} ($\alpha = 1.62$ and $\lambda_{so} = 0$) is also shown with a green dashed line to give a vivid contrast. Generally, the α and λ_{so} are always equal to zero for conventional BCS superconductors where the upper critical field is much lower than the Pauli limit [41]. This suggests that the spin paramagnetic effect and spin-orbit scattering are important to describe the upper critical field for the material. The appearances of large $\mu_0 H_{c2}(0)$ and deviation of the WHH model for conventional BCS superconductors ($\alpha = 0$ and $\lambda_{so} = 0$) are also observed in several cases: noncentrosymmetric superconductors [38], heavy-fermion superconductors [44,45], iron-based high-temperature superconductors [46–52], and deficiencies-induced strong spin-orbit scattering system [53]. The first three scenarios can be easily excluded from our material, and we argue that spin-orbit scattering plays an important role in enhancing the upper critical field for the reason of the large value of λ_{so} here and polycrystalline samples suffering in the dirty limit.

The obtained $\mu_0 H_{c2}(0)$ is used to determine the Ginzburg-Landau coherence length ξ_{GL} from the following relation:

$$\mu_0 H_{c2}(0) = \frac{\Phi_0}{2\pi \xi_{GL}^2(0)},$$

where $\Phi_0 = h/2e$ is the magnetic flux quantum. This leads to the ξ_{GL} 48.14 Å, a distinctly shorter coherence length than other kagome superconductors, such as $LaRu_3Si_2 \sim 107$ Å [54], $LaIr_3Ga_2 \sim 85$ Å [33], and $Mg_2Ir_3Si \sim 74$ Å [27]. Employing the results of ξ_{GL} and $\mu_0 H_{c1}(0)$ calculated previously, the magnetic penetration depth $\lambda_{GL} = 4960.45$ Å is estimated using the following equation:

$$\mu_0 H_{c1} = \frac{\Phi_0}{4\pi \lambda_{GL}^2} \ln \frac{\lambda_{GL}}{\xi_{GL}}.$$

Then the Ginzburg-Landau parameter $\kappa_{GL} = \lambda_{GL}/\xi_{GL} = 103.03 > 1/\sqrt{2}$ confirms that the material is a type-II superconductor. Using the result of $\mu_0 H_{c1}(0)$, $\mu_0 H_{c2}(0)$, and κ_{GL}, the thermodynamic critical field H_c is determined from the relation

$$H_{c1} H_{c2} = H_c^2 \ln \kappa_{GL},$$

which yields $\mu_0 H_c(0) = 97.45$ mT.

The temperature dependence of specific heat $C_p(T)$ measurement is performed to finally confirm the bulk superconducting nature of the material. No anomaly, such as CDW transition in AV_3Sb_5 (A = K, Rb, Cs) [11], is observed above the superconducting transition temperature, as shown in the inset of Fig. 3(c). Low-temperature data with applied field from 0 to 3 T exhibits an obvious anomaly that shifts to lower temperatures with increased fields, corresponding to the emergence of superconducting transition, as shown in

Fig. 3(c). The $C_p(T)$ data at 3 T is described (purple solid line) by the following relation:

$$\frac{C_p}{T} = \gamma_e + \beta T^2 + \eta T^4,$$

where $\gamma_e T$ is the electronic contribution and $\beta T^3 + \eta T^5$ is the phonon contribution to the specific heat. The fitting yields $\gamma_e = 23.7(9)\,\mathrm{mJ\,mol^{-1}\,K^{-2}}$, $\beta = 0.018(2)\,\mathrm{mJ\,mol^{-1}\,K^{-4}}$, and $\eta = 0.0003(1)\,\mathrm{mJ\,mol^{-1}\,K^{-6}}$. The Debye temperature Θ_D can be calculated using the value of β and the equation

$$\Theta_\mathrm{D} = \left(\frac{12\pi^4}{5\beta} nR\right)^{1/3},$$

which gives the Θ_D 409.2(5) K. Combining the $\Theta_\mathrm{D} =$ 409.2 K and $T_c = 7.5$ K [determined from the $4\pi\chi(T)$ curve], the electron-phonon coupling strength λ_ep can be calculated by using the McMillian equation [55]:

$$\lambda_\mathrm{ep} = \frac{1.04 + \mu^* \ln\left(\frac{\Theta_\mathrm{D}}{1.45T_c}\right)}{(1 - 0.62\mu^*)\ln\left(\frac{\Theta_\mathrm{D}}{1.45T_c}\right) - 1.04},$$

where μ^* is a typical value of 0.13. The calculated value of λ_ep is 0.66, suggesting a moderate-coupled superconductor. The density of electronic states at the Fermi energy $N(E_\mathrm{F})$ can be obtained from the following relation [38]:

$$N(E_\mathrm{F}) = \frac{3\gamma_e}{\pi^2 k_\mathrm{B}^2 (1 + \lambda_\mathrm{ep})},$$

where k_B is the Boltzmann constant. Employing the obtained values of $\gamma_e = 23.7\,\mathrm{mJ\,mol^{-1}\,K^{-2}}$ and $\lambda_\mathrm{ep} = 0.66$, the $N(E_\mathrm{F})$ is estimated to be 5.89 states $\mathrm{eV^{-1}}$ per formula unit (f.u.). The relatively large $N(E_\mathrm{F})$ is consistent with the existence of a Van Hove singularity band near the Fermi energy (discussed in the electronic structure part). The mean free path l is estimated from the relation [56]

$$l = 2.732 \times 10^{-14} \frac{\left(\frac{m^*}{m_e}\right) V_M^2}{N(E_\mathrm{F})^2 \rho_0},$$

where V_M, m^*, and m_e are the molar volume, the effective mass of the individual quasiparticles, and the free-electron mass, respectively. Inserting $(\frac{m^*}{m_e}) = 1$ and the obtained $N(E_\mathrm{F})$ and ρ_0 into the above expression gives $l = 0.5$ Å, which is far less than $\xi_\mathrm{GL} = 48.14$ Å. Therefore, the sample is within the dirty limit.

To inspect the pairing symmetry and the magnitude of the specific-heat jump corresponding to the superconducting state ΔC, we obtain ΔC by subtracting the normal state value (the fitting line) from the zero-field data $C(0\ \mathrm{T})$, $\Delta C = C(0T) - C_\mathrm{fit} = C_\mathrm{es} - \gamma_n T$, as shown in Fig. 3(d), where C_es is the superconducting quasiparticle contribution and the γ_n presents the normal state Sommerfeld coefficient of the superconducting part [39,57]. The entropy of the superconducting state S_es is expressed by the following equation:

$$S_\mathrm{es} = -\frac{3\gamma_n}{k_\mathrm{B}\pi^3} \int_0^{2\pi} \int_0^{\infty} [(1-f)\ln(1-f) + f\ln f] d\varepsilon d\phi,$$

where f is the quasiparticle occupation function $f = (1 + e^{E/k_\mathrm{B}T})^{-1}$ and $E = \sqrt{\varepsilon^2 + \Delta^2(\phi)}$. $\Delta(\phi) = \alpha\Delta_\mathrm{BCS}(T)$ is the angle-independent gap function for an s-wave superconductor. Here $\Delta_\mathrm{BCS}(T)$ is the weak-coupled BCS gap function. The electronic specific heat is calculated by $C_\mathrm{es} = T(\partial S_\mathrm{es}/\partial T)$. The experimental data are fitted by the s-wave model, resulting in $\alpha = 1.12$, $\gamma_n = 3.1\,\mathrm{mJ\,mol^{-1}\,K^{-2}}$, and $T_c = 7.47$ K. The normalized specific heat jump $\Delta C/\gamma_n\ T_c$ is obtained to be 1.85, a larger value than the expected value of 1.43 for a weak-coupled BCS superconductor. Meanwhile, the value of $2\Delta(0)/k_\mathrm{B}T_c$ is calculated to be 3.93, which is also larger than the BCS theory value of 3.52. A summary of all the obtained superconducting parameters is in Table II.

TABLE II. Superconductivity parameters of $Ta_2V_{3.1}Si_{0.9}$.

Parameter	Units	$Ta_2V_{3.1}Si_{0.9}$
T_c	K	7.5 (from $4\pi\chi$-T)
$\mu_0 H_{c1}(0)$	mT	3.13(6)
$\mu_0 H_{c2}(0)$	T	14.2
$\mu_0 H_c(0)$	mT	97.45
$\mu_0 H_p(0)$	T	14.985
ξ_GL	Å	48.14
λ_GL	Å	4960.45
κ_GL		103.03
l	Å	0.50
γ_e	$\mathrm{mJ\,mol^{-1}\,K^{-2}}$	23.7(9)
$\Delta C/\gamma_n T_c$		1.85
λ_ep		0.66
$N(E_\mathrm{F})$	state $\mathrm{eV^{-1}}$ per f.u.	5.89
Θ_D	K	409.2
$\Delta(0)$	meV	1.27
$2\Delta(0)/k_\mathrm{B}T_c$		3.93

To better understand the properties of $Ta_2V_{3.1}Si_{0.9}$, we performed the DFT calculations for the pristine (Ta_2V_3Si) and V-doped ($Ta_2V_{3.1}Si_{0.9}$) crystals. Their band structures are presented in Figs. 4(a) and 4(b), respectively. The density of states (DOS) of $Ta_2V_{3.1}Si_{0.9}$ is shown in Fig. 4(b) as well. In the orbital-weighted band structure of Fig. 4(a), one can find that a VHS band is mainly from the V-d_{yz} states, which is about 200 meV above the Fermi energy (E_F). In the $Ta_2V_{3.1}Si_{0.9}$, this VHS band significantly shifts downward and is located at E_F, highlighted by a blue arrow. To elucidate the critical role of the VHS in the emergence of superconductivity, we conduct comprehensive low-temperature measurements of Ta_2V_3Si, as shown in Figs. S1 and S2 of the Supplemental Material (SM) [58]. Although the magnetic susceptibility and resistivity show superconductivity at 5.1 and 6.0 K, respectively, such low superconducting volume fraction and the absence of obvious specific heat jump meticulously demonstrate that the Ta_2V_3Si is not a bulk superconductor. Moreover, the d states from V atoms are predominant in the DOS, indicating the significant role of d electrons of the V breathing kagome lattice for the electronic properties of $Ta_2V_{3.1}Si_{0.9}$. The calculated DOS (E_F) value is 4.88 states/eV per f.u., which generally coincides with the value presented in Table II. The constant energy surfaces of the band at E_F are plotted in the top of Fig. 4(c); the bottom shows isoenergy surfaces at $E = E_\mathrm{F} - 0.118$ eV, being the level of the M point of the VHS band.

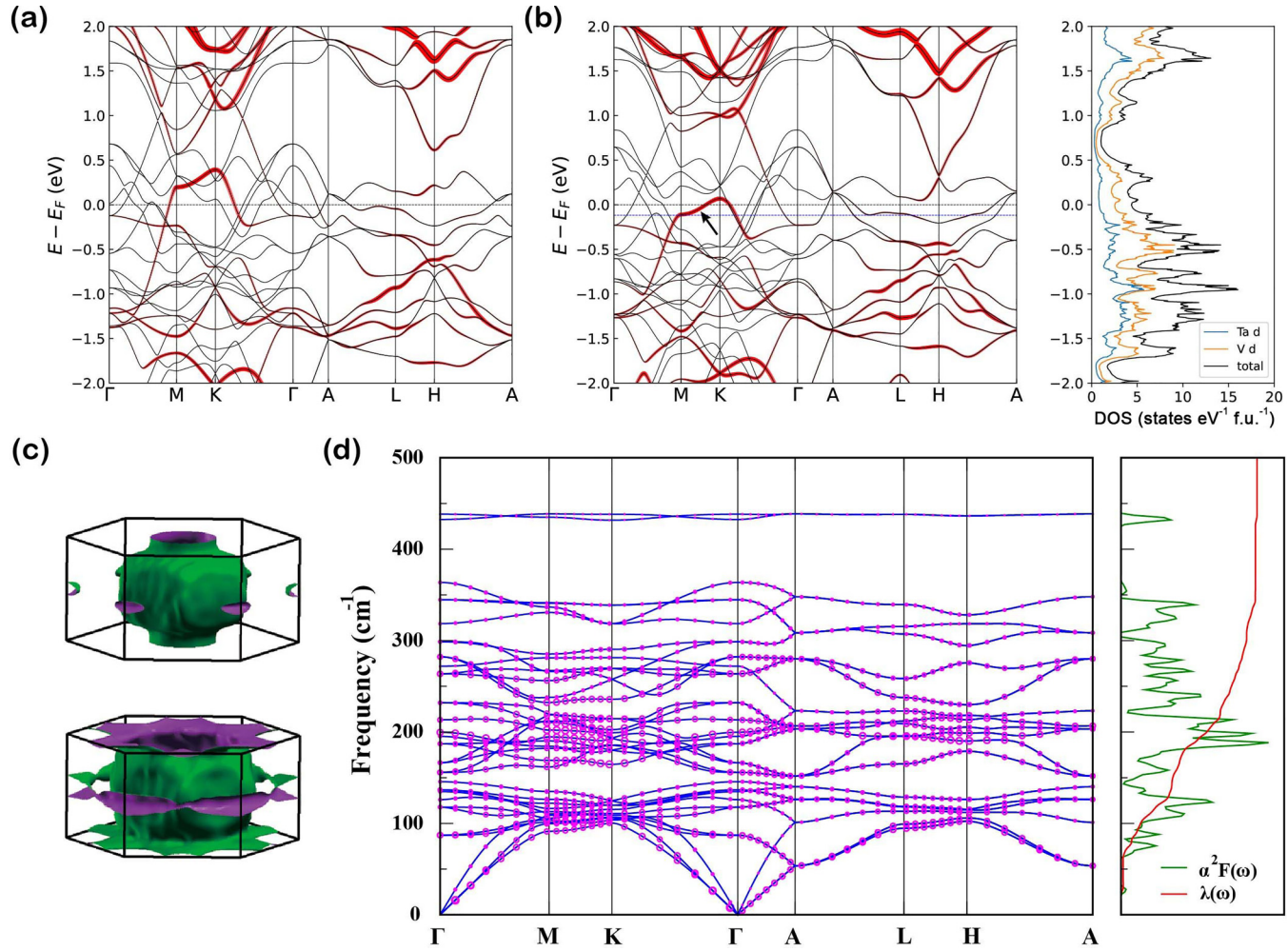

FIG. 4. The DFT calculations of Ta_2V_3Si and $Ta_2V_{3.1}Si_{0.9}$. (a) The orbital-resolved band structure (Ta_2V_3Si) of V atoms' local d_{yz} orbitals. (b) The band structure and density of states of $Ta_2V_{3.1}Si_{0.9}$. The VHS band (29th band at M-K pointed out by the arrow) drops to E_F with doping. The horizontal black and blue dashed lines are situated at E_F and $E_F - 0.118$ eV, respectively. (c) The isoenergy surface at $E = E_F$ (above) and $E = E_F - 0.118$ eV (below) of the 29th band of $Ta_2V_{3.1}Si_{0.9}$. (d) The phonon spectrum, Eliashberg spectral functions $\alpha^2F(\omega)$, and the frequency-dependent coupling $\lambda(\omega)$ of $Ta_2V_{3.1}Si_{0.9}$. The electron-phonon couplings λ_{qv} are depicted by magenta circles.

The superconducting transition temperature is estimated using the Allen-Dynes modified McMillian equation:

$$T_c = \frac{\omega_{\log}}{1.2k_B}\exp\left[\frac{-1.04(1+\lambda)}{\lambda(1-0.62\mu^*)-\mu^*}\right],$$

where k_B is the Boltzmann constant and μ^* is the effective screened Coulomb repulsion constant. $\lambda = \sum_{qv}\lambda_{qv} = 2\int_0^\infty d\omega\frac{\alpha^2F(\omega)}{\omega}$ is the electron-phonon coupling constant, and $\omega_{\log}$ is the logarithmic average phonon frequency. With $\mu^* = 0.1$ and $\lambda = 0.5794$, T_c is estimated to be 4.87 K, which is slightly smaller than the experimental value. The phonon spectrum, Eliashberg spectral functions $\alpha^2F(\omega)$, and the frequency-dependent coupling $\lambda(\omega)$ of $Ta_2V_{3.1}Si_{0.9}$ are shown in Fig. 4(d). The contributions of λ mainly come from the phonon modes of 180 cm^{-1} $< \omega <$ 220 cm^{-1}, which are the in-plane vibration modes of V atoms (see Fig. S3 in the SM [58]).

IV. CONCLUSION

In summary, we investigate the structure and superconductivity of $Ta_2V_{3.1}Si_{0.9}$. The material crystallizes in the layered hexagonal structure with an isolated breathing kagome plane of vanadium atoms. Comprehensive measurements of magnetism, resistivity, and specific heat demonstrate that $Ta_2V_{3.1}Si_{0.9}$ is a moderate-coupled superconductor with a critical temperature of 7.5 K. Although most of the physical properties are close to the BCS theory, the large upper critical field, distinct spin paramagnetic effect, and spin-orbit scattering suggest an unusual pairing mechanism. Moreover, DFT calculations depict a VHS band deriving from the V-d_{yz} states locates at E_F, which is also observed in CsV_3Sb_5 and plays an important role in the formations of superconductivity and CDW order [59,60]. The electron-phonon coupling calculation reveals that the in-plane vibrations of V atoms mainly contribute to the observed superconductivity. Our study provides a platform to research the interplay between geometrical frustration and superconductivity in the V-based kagome

lattice. To further explore the novel phenomena in this material, such as nontrivial topological band structure, CDW order, time-reversal symmetry breaking, and PDW observed in another V-based kagome superconductor AV_3Sb_5, the single crystals of $Ta_2V_{3.1}Si_{0.9}$ are urgently needed.

ACKNOWLEDGMENTS

We would like to thank Y. Zhou for the helpful discussion and careful reading of the manuscript. This work was financially supported by the National Key Research and Development Program of China (Grants No. 2022YFA1403400 and No. 2022YFA1403800), the Natural Science Foundation of China (Grants No. U2032204, No. U22A6005, No. 12188101, No. 11974395, and No. 12104492), the Strategic Priority Research Program of the Chinese Academy of Sciences (Grant No. XDB33010000), The China Postdoctoral Science Foundation (Grant No. 2021TQ0356), the Informatization Plan of Chinese Academy of Sciences (Grant No. CAS-WX2021SF-0102), the Synergetic Extreme Condition User Facility (SECUF), and the Center for Materials Genome.

[1] P. W. Anderson, Resonating valence bonds: A new kind of insulator?, Mater. Res. Bull. **8**, 153 (1973).
[2] P. A. Lee, An end to the drought of quantum spin liquids, Science **321**, 1306 (2008).
[3] C. Broholm, R. J. Cava, S. A. Kivelson, D. G. Nocera, M. R. Norman, and T. Senthil, Quantum spin liquids, Science **367**, eaay0668 (2020).
[4] J. Knolle and R. Moessner, A field guide to spin liquids, Annu. Rev. Condens. Matter Phys. **10**, 451 (2019).
[5] Y. Zhou, K. Kanoda, and T.-K. Ng, Quantum spin liquid states, Rev. Mod. Phys. **89**, 025003 (2017).
[6] M. R. Norman, Colloquium: Herbertsmithite and the search for the quantum spin liquid, Rev. Mod. Phys. **88**, 041002 (2016).
[7] L. Balents, Spin liquids in frustrated magnets, Nature (London) **464**, 199 (2010).
[8] J. X. Yin, B. Lian, and M. Z. Hasan, Topological kagome magnets and superconductors, Nature (London) **612**, 647 (2022).
[9] W. S. Wang, Z. Z. Li, Y. Y. Xiang, and Q. H. Wang, Competing electronic orders on kagome lattices at van Hove filling, Phys. Rev. B **87**, 115135 (2013).
[10] M. L. Kiesel, C. Platt, and R. Thomale, Unconventional Fermi Surface Instabilities in the Kagome Hubbard Model, Phys. Rev. Lett. **110**, 126405 (2013).
[11] B. R. Ortiz, L. C. Gomes, J. R. Morey, M. Winiarski, M. Bordelon, J. S. Mangum, L. W. H. Oswald, J. A. Rodriguez-Rivera, J. R. Neilson, S. D. Wilson, E. Ertekin, T. M. McQueen, and E. S. Toberer, New kagome prototype materials: Discovery of KV_3Sb_5, RbV_3Sb_5, and CsV_3Sb_5, Phys. Rev. Mater. **3**, 094407 (2019).
[12] B. R. Ortiz, S. M. L. Teicher, Y. Hu, J. L. Zuo, P. M. Sarte, E. C. Schueller, A. M. M. Abeykoon, M. J. Krogstad, S. Rosenkranz, R. Osborn, R. Seshadri, L. Balents, J. He, and S. D. Wilson, CsV_3Sb_5: A Z_2 Topological Kagome Metal with a Superconducting Ground State, Phys. Rev. Lett. **125**, 247002 (2020).
[13] B. R. Ortiz, P. M. Sarte, E. M. Kenney, M. J. Graf, S. M. L. Teicher, R. Seshadri, and S. D. Wilson, Superconductivity in the Z_2 kagome metal KV_3Sb_5, Phys. Rev. Mater. **5**, 034801 (2021).
[14] Q. W. Yin, Z. J. Tu, C. S. Gong, Y. Fu, S. H. Yan, and H. C. Lei, Superconductivity and normal-state properties of kagome metal RbV_3Sb_5 single crystals, Chin. Phys. Lett. **38**, 037403 (2021).
[15] S. Y. Yang, Y. Wang, B. R. Ortiz, D. Liu, J. Gayles, E. Derunova, R. Gonzalez-Hernandez, L. Smejkal, Y. Chen, S. S. P. Parkin, S. D. Wilson, E. S. Toberer, T. McQueen, and M. N. Ali, Giant, unconventional anomalous Hall effect in the metallic frustrated magnet candidate, KV_3Sb_5, Sci. Adv. **6**, eabb6003 (2020).
[16] Y. X. Jiang, J. X. Yin, M. M. Denner, N. Shumiya, B. R. Ortiz, G. Xu, Z. Guguchia, J. He, M. S. Hossain, X. Liu, J. Ruff, L. Kautzsch, S. S. Zhang, G. Chang, I. Belopolski, Q. Zhang, T. A. Cochran, D. Multer, M. Litskevich, Z. J. Cheng *et al.*, Unconventional chiral charge order in kagome superconductor KV_3Sb_5, Nat. Mater. **20**, 1353 (2021).
[17] H. Luo, Q. Gao, H. Liu, Y. Gu, D. Wu, C. Yi, J. Jia, S. Wu, X. Luo, Y. Xu, L. Zhao, Q. Wang, H. Mao, G. Liu, Z. Zhu, Y. Shi, K. Jiang, J. Hu, Z. Xu, and X. J. Zhou, Electronic nature of charge density wave and electron-phonon coupling in kagome superconductor KV_3Sb_5, Nat. Commun. **13**, 273 (2022).
[18] C. Mielke 3rd, D. Das, J. X. Yin, H. Liu, R. Gupta, Y. X. Jiang, M. Medarde, X. Wu, H. C. Lei, J. Chang, P. Dai, Q. Si, H. Miao, R. Thomale, T. Neupert, Y. Shi, R. Khasanov, M. Z. Hasan, H. Luetkens, and Z. Guguchia, Time-reversal symmetry-breaking charge order in a kagome superconductor, Nature (London) **602**, 245 (2022).
[19] S. Cho, H. Ma, W. Xia, Y. Yang, Z. Liu, Z. Huang, Z. Jiang, X. Lu, J. Liu, Z. Liu, J. Li, J. Wang, Y. Liu, J. Jia, Y. Guo, J. Liu, and D. Shen, Emergence of New Van Hove Singularities in the Charge Density Wave State of a Topological Kagome Metal RbV_3Sb_5, Phys. Rev. Lett. **127**, 236401 (2021).
[20] C. Mu, Q. Yin, Z. Tu, C. Gong, H. Lei, Z. Li, and J. Luo, S-Wave superconductivity in kagome metal CsV_3Sb_5 revealed by 121/123Sb NQR and 51V NMR measurements, Chin. Phys. Lett. **38**, 077402 (2021).
[21] W. Y. Duan, Z. Y. Nie, S. S. Luo, F. H. Yu, B. R. Ortiz, L. C. Yin, H. Su, F. Du, A. Wang, Y. Chen, X. Lu, J. J. Ying, S. D. Wilson, X. H. Chen, Y. Song, and H. Q. Yuan, Nodeless superconductivity in the kagome metal CsV_3Sb_5, Sci. China: Phys. Mech. Astron. **64**, 107462 (2021).
[22] L. S. W. C. C. Zhao, W. Xia, Q. W. Yin, J. M. Ni, Y. Y. Huang, C. P. Tu, Z. C. Tao, Z. J. Tu, C. S. Gong, H. C. Lei, Y. F. Guo, X. F. Yang, and S. Y. Li, Nodal superconductivity and superconducting domes in the topological Kagome metal CsV_3Sb_5, arXiv:2102.08356.
[23] H. S. Xu, Y. J. Yan, R. Yin, W. Xia, S. Fang, Z. Chen, Y. Li, W. Yang, Y. Guo, and D. L. Feng, Multiband Superconductivity with Sign-Preserving Order Parameter in Kagome Superconductor CsV_3Sb_5, Phys. Rev. Lett. **127**, 187004 (2021).
[24] Z. Liang, X. Hou, F. Zhang, W. Ma, P. Wu, Z. Zhang, F. Yu, J. J. Ying, K. Jiang, L. Shan, Z. Wang, and X. H. Chen, Three-Dimensional Charge Density Wave and Surface-Dependent Vortex-Core States in a Kagome Superconductor CsV_3Sb_5, Phys. Rev. X **11**, 031026 (2021).

[25] H. Chen, H. Yang, B. Hu, Z. Zhao, J. Yuan, Y. Xing, G. Qian, Z. Huang, G. Li, Y. Ye, S. Ma, S. Ni, H. Zhang, Q. Yin, C. Gong, Z. Tu, H. Lei, H. Tan, S. Zhou, C. Shen *et al.*, Roton pair density wave in a strong-coupling kagome superconductor, Nature (London) **599**, 222 (2021).

[26] J. T. Jin, K. Jiang, H. Yao, and Y. Zhou, Interplay between Pair Density Wave and a Nested Fermi Surface, Phys. Rev. Lett. **129**, 167001 (2022).

[27] K. Kudo, H. Hiiragi, T. Honda, K. Fujimura, H. Idei, and M. Nohara, Superconductivity in Mg_2Ir_3Si: A fully ordered laves phase, J. Phys. Soc. Jpn. **89**, 013701 (2020).

[28] H. C. Ku, G. P. Meisner, F. Acker, and D. C. Johnston, Superconducting and magnetic-properties of new ternary borides with the $CeCo_3B_2-$Type structure, Solid State Commun. **35**, 91 (1980).

[29] K. S. Athreya, L. S. Hausermannberg, R. N. Shelton, S. K. Malik, A. M. Umarji, and G. K. Shenoy, Superconductivity in the ternary borides $CeOs_3B_2$ and $CeRu_3B_2$ - magnetic-susceptibility and specific-heat measurements, Phys. Lett. A **113**, 330 (1985).

[30] S. Li, B. Zeng, X. G. Wan, J. Tao, F. Han, H. Yang, Z. H. Wang, and H. H. Wen, Anomalous properties in the normal and superconducting states of $LaRu_3Si_2$, Phys. Rev. B **84**, 214527 (2011).

[31] S. Li, J. Xing, J. Tao, H. Yang, and H. H. Wen, Superconductivity in $Ba_{2/3}Pt_3B_2$ with the kagome lattice, Ann. Phys. **358**, 248 (2015).

[32] S. Chaudhary, J. Singh Shama, A. Consiglio, D. Di Sante, R. Thomale, and Y. Singh, Role of electronic correlations in the kagome-lattice superconductor $LaRh_3B_2$, Phys. Rev. B **107**, 085103 (2023).

[33] X. Gui and R. J. Cava, $LaIr_3Ga_2$: A superconductor based on a kagome lattice of Ir, Chem. Mater. **34**, 2824 (2022).

[34] C. S. Gong, S. J. Tian, Z. J. Tu, Q. W. Yin, Y. Fu, R. T. Luo, and H. C. Lei, Superconductivity in kagome metal YRu_3Si_2 with strong electron correlations, Chin. Phys. Lett. **39**, 087401 (2022).

[35] B. H. Toby and R. B. Von Dreele, GSAS-II: The genesis of a modern open-source all-purpose crystallography software package, J. Appl. Crystallogr. **46**, 544 (2013).

[36] R. C. Mittal, S. K. Si, and K. P. Gupta, Si-Stabilised C14 laves phases in the transition metal systems, J. Less-Common Met. **60**, 75 (1978).

[37] K. Momma and F. Izumi, VESTA 3 for three-dimensional visualization of crystal, volumetric and morphology data, J. Appl. Crystallogr. **44**, 1272 (2011).

[38] E. M. Carnicom, W. Xie, T. Klimczuk, J. Lin, K. Gornicka, Z. Sobczak, N. P. Ong, and R. J. Cava, $TaRh_2B_2$ and $NbRh_2B_2$: Superconductors with a chiral noncentrosymmetric crystal structure, Sci. Adv. **4**, eaar7969 (2018).

[39] D. Y. Yan, M. Yang, C. X. Wang, P. B. Song, C. J. Yi, and Y. G. Shi, Superconductivity in centrosymmetric topological superconductor candidate TaC, Supercond. Sci. Technol. **34**, 035025 (2021).

[40] N. R. Werthamer, E. Helfand, and P. C. Hohenberg, Temperature and purity dependence of the superconducting critical field, Hc_2. III. Electron spin and spin-orbit effects, Phys. Rev. **147**, 295 (1966).

[41] D. Y. Yan, D. Y. Geng, Q. Gao, Z. H. Cui, C. J. Yi, Y. Feng, C. Y. Song, H. L. Luo, M. Yang, M. Arita, S. Kumar, E. F. Schwier, K. Shimada, L. Zhao, K. H. Wu, H. M. Weng, L. Chen, X. J. Zhou, Z. J. Wang, Y. G. Shi, and B. J. Feng, Superconductivity and Fermi-surface nesting in the candidate Dirac semimetal NbC, Phys. Rev. B **102**, 205117 (2020).

[42] K. Maki, The magnetic properties of superconducting alloys. II, Phys. Phys. Fiz. **1**, 127 (1964).

[43] K. Maki, Effect of Pauli paramagnetism on magnetic properties of high-field superconductors, Phys. Rev. **148**, 362 (1966).

[44] A. D. Bianchi, M. Kenzelmann, L. Debeer-Schmitt, J. S. White, E. M. Forgan, J. Mesot, M. Zolliker, J. Kohlbrecher, R. Movshovich, E. D. Bauer, J. L. Sarrao, Z. Fisk, C. Petrovic, and M. R. Eskildsen, Superconducting vortices in $CeCoIn_5$: Toward the pauli-limiting field, Science **319**, 177 (2008).

[45] E. Campillo, R. Riyat, S. Pollard, P. Jefferies, A. T. Holmes, R. Cubitt, J. S. White, J. Gavilano, Z. Huesges, O. Stockert, E. M. Forgan, and E. Blackburn, Observations of the effect of strong Pauli paramagnetism on the vortex lattice in superconducting $CeCu_2Si_2$, Phys. Rev. B **104**, 184508 (2021).

[46] G. Fuchs, S. L. Drechsler, N. Kozlova, G. Behr, A. Kohler, J. Werner, K. Nenkov, R. Klingeler, J. Hamann-Borrero, C. Hess, A. Kondrat, M. Grobosch, A. Narduzzo, M. Knupfer, J. Freudenberger, B. Buchner, and L. Schultz, High-field Pauli-limiting Behavior and Strongly Enhanced Upper Critical Magnetic Fields Near the Transition Temperature of an Arsenic-Deficient $LaO_{0.9}F_{0.1}FeAs_{1-\delta}$ Superconductor, Phys. Rev. Lett. **101**, 237003 (2008).

[47] S. Khim, J. W. Kim, E. S. Choi, Y. Bang, M. Nohara, H. Takagi, and K. H. Kim, Evidence for dominant Pauli paramagnetic effect in the upper critical field of single-crystalline $FeTe_{0.6}Se_{0.4}$, Phys. Rev. B **81**, 184511 (2010).

[48] H. Lei, R. Hu, E. S. Choi, J. B. Warren, and C. Petrovic, Pauli-limited upper critical field of $Fe_{1+y}Te_{1-x}Se_x$, Phys. Rev. B **81**, 094518 (2010).

[49] S. Khim, B. Lee, J. W. Kim, E. S. Choi, G. R. Stewart, and K. H. Kim, Pauli-limiting effects in the upper critical fields of a clean LiFeAs single crystal, Phys. Rev. B **84**, 104502 (2011).

[50] Z. Wang, J. Yuan, J. Wosnitza, H. Zhou, Y. Huang, K. Jin, F. Zhou, X. Dong, and Z. Zhao, The upper critical field and its anisotropy in $Li_{1-x}Fe_xOHFe_{1-y}Se$, J Phys.: Condens. Matter **29**, 025701 (2017).

[51] X. Xing, W. Zhou, J. Wang, Z. Zhu, Y. Zhang, N. Zhou, B. Qian, X. Xu, and Z. Shi, Two-band and Pauli-limiting effects on the upper critical field of 112-type iron pnictide superconductors, Sci. Rep. **7**, 45943 (2017).

[52] T. Wang, C. Zhang, L. Xu, J. Wang, S. Jiang, Z. Zhu, Z. Wang, J. Chu, J. Feng, L. Wang, W. Li, T. Hu, X. Liu, and G. Mu, Strong Pauli paramagnetic effect in the upper critical field of $KCa_2Fe_4As_4F_2$, Sci. China: Phys. Mech. Astron. **63**, 227412 (2019).

[53] Y. Lu, T. Takayama, A. F. Bangura, Y. Katsura, D. Hashizume, and H. Takagi, Superconductivity at 6 K and the violation of Pauli limit in $Ta_2Pd_xS_5$, J. Phys. Soc. Jpn. **83**, 023702 (2014).

[54] Y. Kishimoto, T. Ohno, T. Hihara, K. Sumiyama, G. Ghosh, and L. C. Gupta, Magnetic susceptibility study of $LaRu_3Si_2$, J. Phys. Soc. Jpn. **71**, 2035 (2002).

[55] W. L. Mcmillan, Transition temperature of strong-coupled superconductors, Phys. Rev. **167**, 331 (1968).

[56] Y. Singh, C. Martin, S. L. Bud'ko, A. Ellern, R. Prozorov, and D. C. Johnston, Multigap superconductivity and Shubnikov–de Haas oscillations in single crystals of the layered boride OsB_2, Phys. Rev. B **82**, 144532 (2010).

[57] X. Xu, B. Chen, W. H. Jiao, B. Chen, C. Q. Niu, Y. K. Li, J. H. Yang, A. F. Bangura, Q. L. Ye, C. Cao, J. H. Dai, G. Cao, and N. E. Hussey, Evidence for two energy gaps and Fermi liquid behavior in the $SrPt_2As_2$ superconductor, Phys. Rev. B **87**, 224507 (2013).

[58] See Supplemental Material at http://link.aps.org/supplemental/10.1103/PhysRevB.108.104504 for XRD patterns of Ta_2V_3Si and $Ta_2V_3Si_{0.9}$, low-temperature physical properties of Ta_2V_3Si, and the phonon vibration modes that make a significant contribution to the electron-phonon coupling in $Ta_2V_3Si_{0.9}$.

[59] Y. Hu, X. Wu, B. R. Ortiz, S. Ju, X. Han, J. Ma, N. C. Plumb, M. Radovic, R. Thomale, S. D. Wilson, A. P. Schnyder, and M. Shi, Rich nature of Van Hove singularities in Kagome superconductor CsV_3Sb_5, Nat. Commun. **13**, 2220 (2022).

[60] M. G. Kang, S. A. Fang, J. K. Kim, B. R. Ortiz, S. H. Ryu, J. M. Kim, J. Yoo, G. Sangiovanni, D. Di Sante, B. G. Park, C. Jozwiak, A. Bostwick, E. Rotenberg, E. Kaxiras, S. D. Wilson, J. H. Park, and R. Comin, Twofold van Hove singularity and origin of charge order in topological kagome superconductor CsV_3Sb_5, Nat. Phys. **18**, 301 (2022).